

THE LARGEST MOLECULAR CLOUD COMPLEXES IN THE FIRST GALACTIC QUADRANT

T. M. DAME, B. G. ELMEGREEN, R. S. COHEN, AND P. THADDEUS

Goddard Institute for Space Studies; and Columbia University

Received 1985 May 23; accepted 1985 December 4

ABSTRACT

The Columbia CO survey of the first Galactic quadrant was used to determine the locations and physical properties of the largest molecular complexes in the inner Galaxy. Within the range of the survey ($l = 12^\circ$ – 60°), 26 complexes were detected with masses greater than $5 \times 10^5 M_\odot$, and roughly several hundred such complexes are deduced to exist throughout the Galaxy within the solar circle. These complexes are the parent objects of much of the Population I in the Galaxy.

Distances to most of the complexes were determined kinematically, the distance ambiguity being resolved with the aid of associated H II regions, OB associations, masers, and other early Population I objects. The largest complexes are good tracers of spiral structure, the Sagittarius arm in particular being delineated with unprecedented clarity. A total of 17 large complexes are distributed rather uniformly along a 15 kpc stretch of the arm with a spacing comparable to that of the strings of regularly spaced H II regions observed in external galaxies.

Power-law relations exist between the line widths and sizes of the complexes and between their densities and sizes. The forms of these relations are in good agreement with those found previously by ourselves and other observers, and we extend them by roughly an order of magnitude in cloud mass.

Subject headings: galaxies: Milky Way — galaxies: structure — interstellar: molecules

I. INTRODUCTION

A small number of very large, fairly well defined molecular complexes dominate the CO emission within a few kiloparsecs of the Sun. For example, most of the emission in the Perseus spiral arm from $l = 104^\circ$ – 180° , as shown in Figure 1, is contained in the three large complexes associated with the H II regions NGC 7538, W3, and S235. Even though each of these complexes could be decomposed into a number of smaller clouds, Figure 1 leaves very little doubt that each is a single, well-defined object: the overall density of clouds in the Perseus arm is far too low for these to be merely statistical fluctuations in the distribution of smaller clouds. Like Orion (Maddalena *et al.* 1986) and M17 (Elmegreen, Lada, and Dickinson 1979), the complex NGC 7538 is representative of the largest complexes in the solar neighborhood, composed of several loosely connected smaller clumps that are often active star-forming regions; it contains $\sim 10^6 M_\odot$ and has internal motions in excess of 15 km s^{-1} .

Apparently, objects similar to the NGC 7538 cloud complex exist throughout the inner Galaxy. The CO longitude-velocity diagram in Figure 2a, smoothed to highlight the large-scale structure of the emission, is dominated by ~ 30 intense emission features with typical dimensions of 1° – 2° by 10 – 20 km s^{-1} ; these are identified by their Galactic longitudes and velocities in Figure 2b (and in the text these codes appear in brackets). The angular sizes, velocity extents, and apparent CO luminosities of many of these features suggest that they arise from molecular complexes similar to the largest local complexes such as Orion and NGC 7538 and, like them, these features appear closely associated with a variety of early Population I objects (Myers *et al.* 1986). Some of the features identified in Figure 2 are well known, such as [14,20], the large molecular complex at 2.3 kpc associated with the H II region M17 (Elmegreen, Lada, and Dickinson 1979), and [49,59], the complex at 7.3 kpc associated with W51 (Mufson and Liszt

1979). In the following analysis we assume that many of the features in Figure 2b correspond to similar molecular complexes. Because such large complexes can be identified and resolved over large areas of the Galaxy, and because associated Population I objects can help to resolve the kinematic distance ambiguity and locate the complexes in the Galactic plane, the largest complexes are potentially a very powerful probe of Galactic structure.

In this paper we determine the Galactic distribution and physical properties of the largest molecular complexes using the Columbia CO survey of the first Galactic quadrant (Cohen, Dame, and Thaddeus 1986). The basic parameters of the survey are given in Table 1. In § II we discuss the problem of definition—how the largest complexes can be distinguished from the more extended background emission; determine distances, masses, and other physical properties for the complexes; and investigate how such properties vary with cloud size. In § III we discuss the Galactic distribution of the complexes and their relationship to the large-scale structure of the Galaxy, and in § IV consider the completeness of our cloud sample and investigate whether that sample is consistent with what is known about the mass spectrum of molecular clouds and the total molecular mass of the inner Galaxy.

II. ANALYSIS

a) Cloud Definition

Near the Galactic equator, the weak, extended background of CO emission in which the large complexes identified in Figure 2 are immersed—the sum of many smaller or more distant clouds along the line of sight—is a source of confusion or “noise” that makes identification of individual complexes difficult. This background proves particularly troublesome in the molecular-ring region, where overall cloud density is highest, and near the terminal velocity, where velocity crowd-

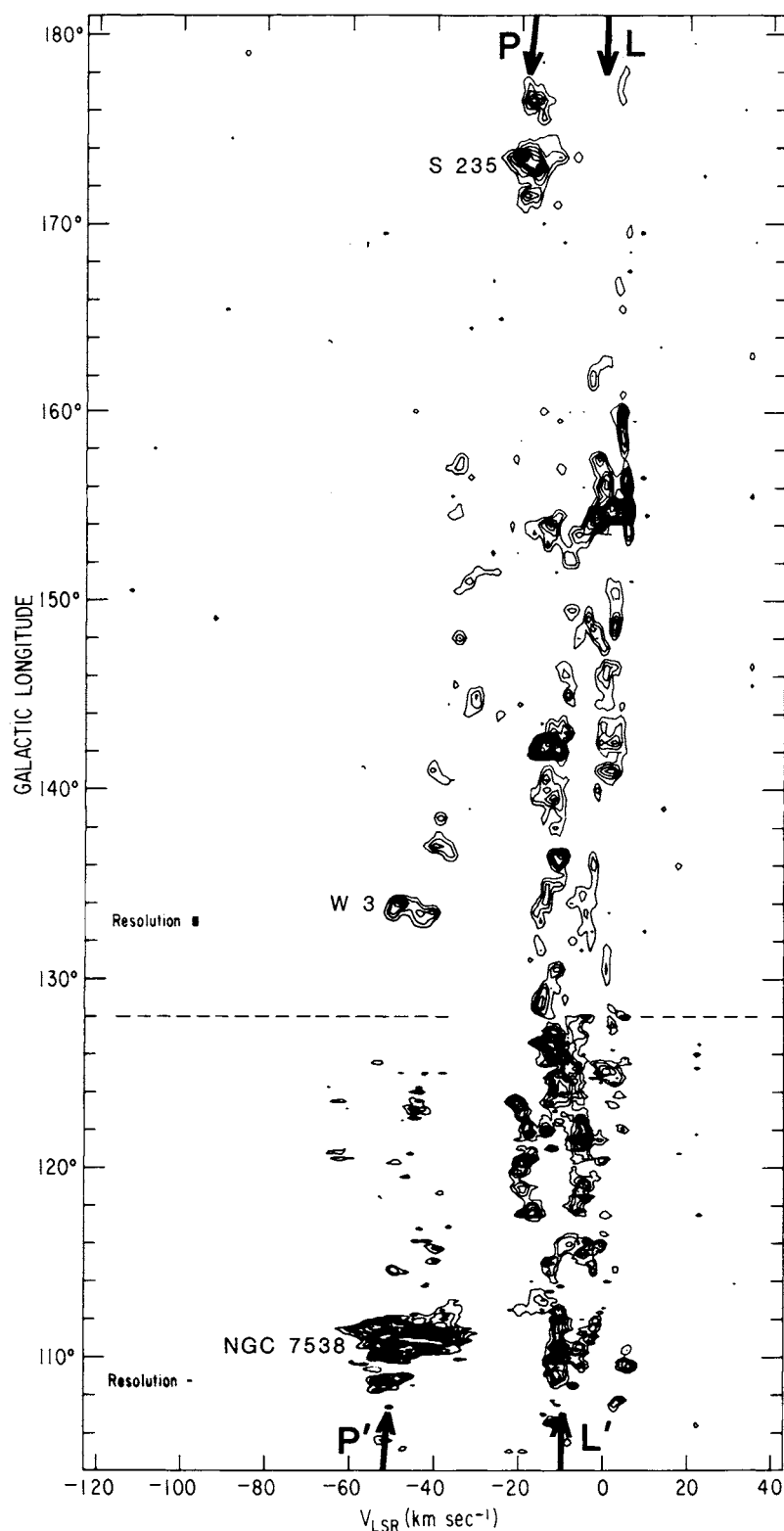


FIG. 1.—Longitude-velocity diagram obtained by integrating the Columbia CO survey of the second Galactic quadrant (Cohen *et al.* 1980) across the Galactic plane. Contours denote equal values of $\int T_R db$, where T_R is antenna temperature corrected for atmospheric absorption and beam efficiency, and b is Galactic latitude; the survey was integrated over $\pm 3^\circ$ in latitude and the contour interval is 0.5 K deg_b (i.e., K times degrees of Galactic latitude). Above $l = 128^\circ$ spectra were taken rapidly, and the survey was smoothed to a longitude resolution of 0.5° to enhance the signal-to-noise ratio. The arrows L and L' point to the Local spiral arm, and the arrows P and P' point to the nearly parallel lane of the Perseus arm. The three largest complexes in the Perseus arm are labeled with the names of associated H II regions.

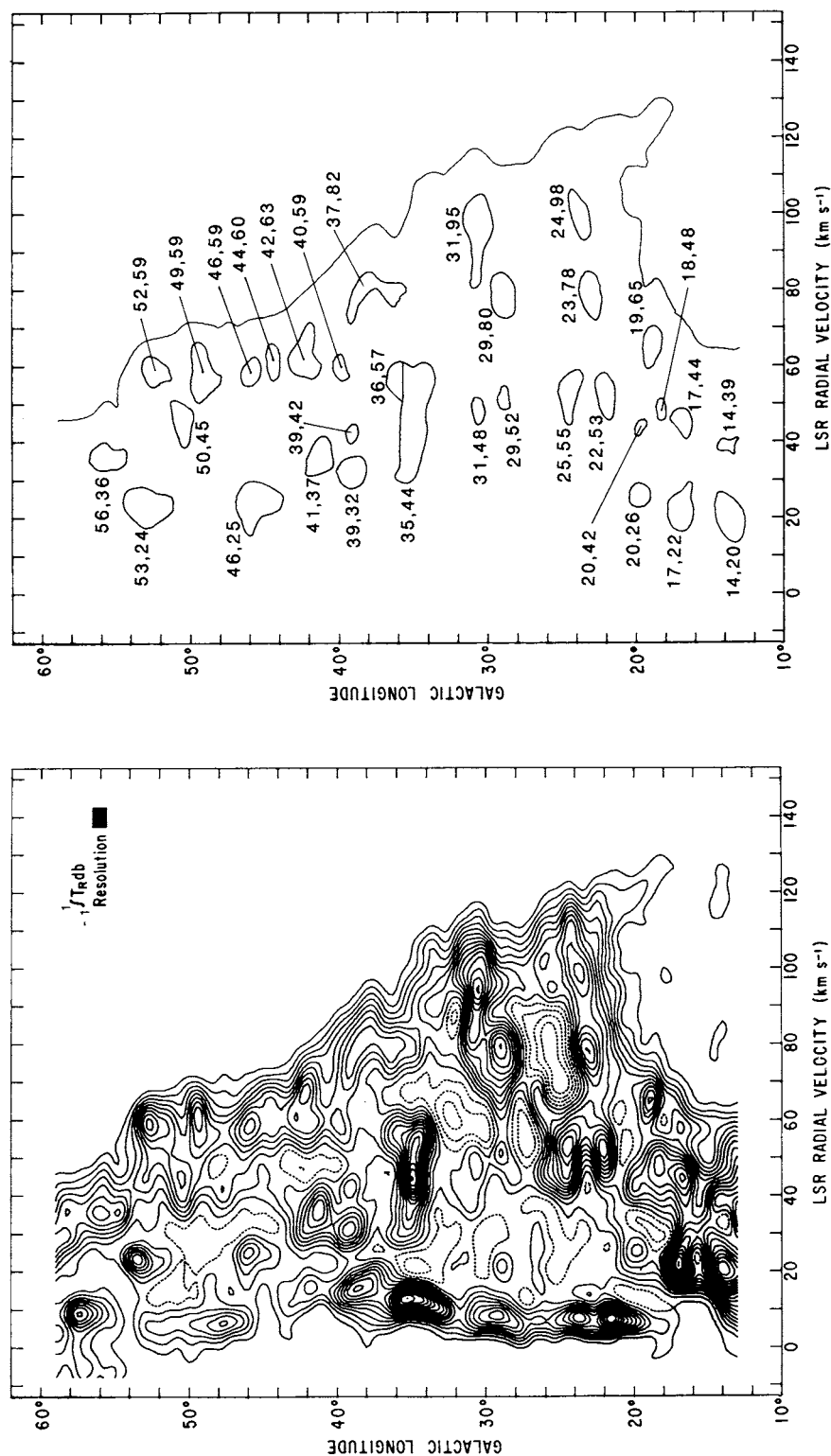


FIG. 2a

FIG. 2b

FIG. 2.—(a) Longitude-velocity diagram obtained by integrating the Columbia CO survey of the first Galactic quadrant (Cohen, Dame, and Thaddeus 1986) over latitude from -1° to $+1^\circ$ and by smoothing to a resolution of 1° by 5.2 km s^{-1} . The contour interval is 0.25 K deg . (b) Key to the main emission features in (a). The positions of the 32 clouds discussed in the text and listed in Table 2 are marked in the longitude-velocity diagram, usually by the last closed contour from (a), identified by longitude and velocity. The emission at $v < 20 \text{ km s}^{-1}$, arising mainly from clouds within 500 pc which extend well beyond the latitude limits of the present survey, is discussed elsewhere (Dame and Thaddeus 1985).

TABLE 1
COLUMBIA CO SURVEY OF THE FIRST QUADRANT

Parameter	Value
Galactic longitude	12° to 60°
Galactic latitude	-1° to 1°
Sampling interval:	
<i>b</i> ≤ 0°5	0°125
<i>b</i> > 0°5	0°25
Radial velocity:	
<i>l</i> ≤ 55°	-13 to 153 km s ⁻¹
<i>l</i> > 55°	-55 to 111 km s ⁻¹
Beamwidth	8'
Velocity resolution	0.65 km s ⁻¹
Sensitivity	<i>T_R</i> = 0.45 K rms at Δ <i>v</i> = 1.3 km s ⁻¹

ing occurs. To determine the Galactic distribution and physical properties of the complexes, initially we must consider precisely how the complexes are defined and how the “chaff” of background emission should be removed.

Smoothing is one effective way to suppress background-

cloud noise and highlight the largest emission features, but Figure 2 alone might allow one to wonder whether many of the features could actually be a consequence of this procedure. The unsmoothed, color-code longitude-velocity diagram in Figure 3 (Plate 13), however, demonstrates that this is not the case. Most of the complexes in this higher resolution diagram, where far more structure is apparent, can be resolved into several components, as would be expected from the fragmented appearance of nearby complexes; yet the main features that dominate the emission here are those identified in Figure 2.

Another way to suppress background emission and allow better definition of the large complexes is to “clip” the data, i.e., to set to zero all spectral channels below some threshold temperature. This procedure yields integrated maps (e.g., velocity-integrated spatial maps or latitude-integrated [*l*, *v*]-maps) that highlight the emission from intense but localized large complexes which weak but extended background would otherwise obscure.

A longitude-velocity diagram integrated over ±1° in latitude and clipped at a threshold of 2 K (Fig. 4) still allows some confusion in the molecular ring region where a higher threshold might have been appropriate, but essentially the same

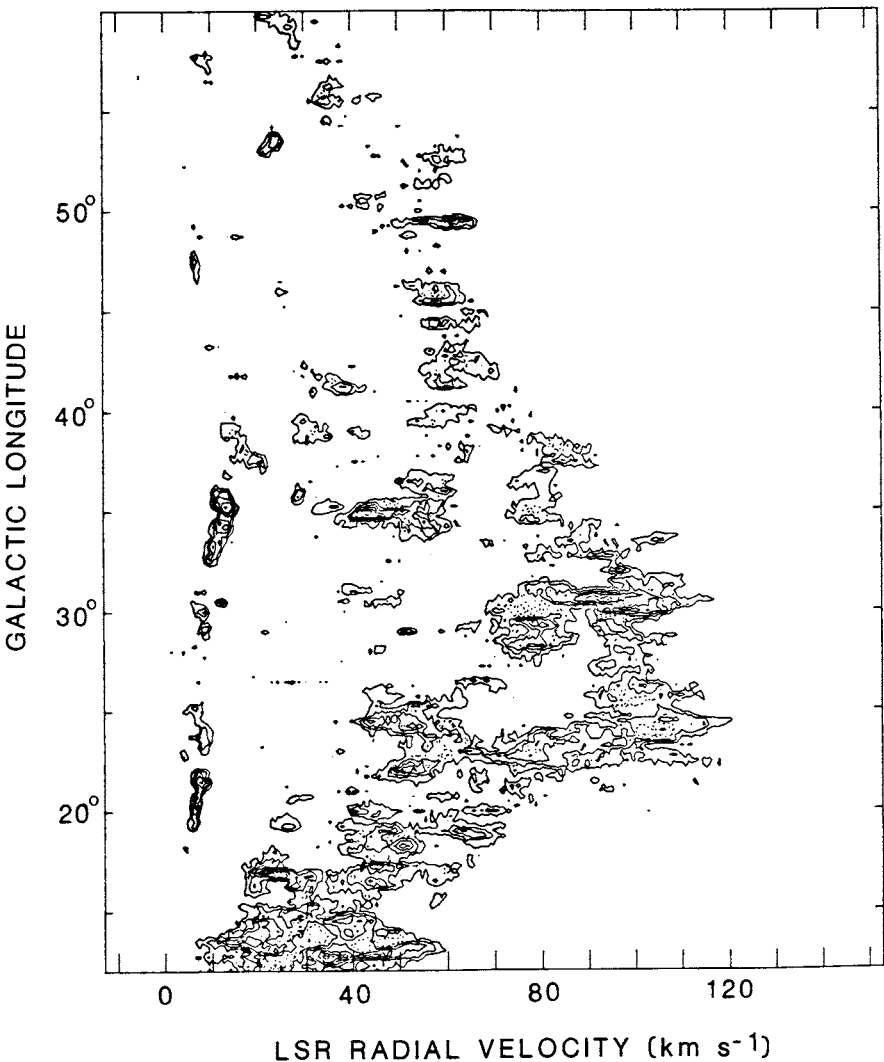


FIG. 4.—Longitude-velocity map obtained by integrating the CO emission with *T* > 2 K over latitude from -1° to +1°. The contour interval is 0.75 K deg.

complexes identified in the smoothed (l, v) -diagram (Fig. 2) stand out and dominate the overall emission here. The similar large-scale structure of the smoothed, unprocessed, and clipped (l, v) -maps (Figs. 2, 3, and 4; see also Appendix B) is strong evidence for the reality of the large complexes: whichever way the data are processed or represented, the same objects appear.

In two typical spatial maps made by clipping at 2 K (Fig. 5), the complexes are well defined and appear similar to the nearby complex in Orion and Monoceros and to the one toward NGC 7538, all of them composed of several fragments which are the main sites of star formation; for example, Figure 5a indicates the position of four H II regions associated with complex [46,59], while Figure 5b indicates the position of an SNR possibly associated with the complex [22,53]. In our discussion we use these particular complexes to illustrate our main methods of determining distances; in § IV we present similar clipped maps of all the complexes.

After identifying the dominant sources in the data, the question remains how to partition the emission between source and background. We removed most of the background emission from the longitude-velocity diagram by assuming that the background clouds in the Galactic plane are symmetric about the Galactic center and have the same radial distribution as the overall CO emission (the so-called "molecular-ring" distribution). A model longitude-velocity diagram of the background emission, constructed using these simple assumptions, was subtracted from the observed diagram (Fig. 3). Once the appropriate background level was chosen, most of the complexes in the residual diagram (Fig. 11) were well separated, and their integrated CO intensities could be determined with little ambiguity. The details of the method are discussed in Appendix B.

b) Individual Cloud Properties

i) Mass

The mass of each complex was determined directly from its total CO emission by assuming a proportionality between integrated CO line intensity, $W(\text{CO}) = \int T(\text{CO})dv$, and H_2 column density, $N(\text{H}_2)$. Because the CO $1 \rightarrow 0$ line is often optically

thick in molecular clouds, such proportionality was not predicted on the basis of simple radiative transfer models of cloud structure, and it is still not entirely understood. Its justification is almost entirely empirical: the finding by many observers (e.g., Kutner *et al.* 1977) that the CO $1 \rightarrow 0$ line profiles in molecular clouds are generally constant multiples of those of the same transition of ^{13}CO and C^{18}O , which, being far less saturated, are thought to trace the mass in molecular clouds. It appears that ^{12}CO can be used as a rough mass tracer in molecular clouds because $W(\text{CO})$ is an average over many small clumps which, like the clouds as a whole in the Galactic plane, do not seriously shadow one another in space and velocity. The very clumpy nature of the large complexes is implied by their low mean H_2 density of $\sim 10 \text{ cm}^{-3}$ (see § IIc), about two orders of magnitude lower than the density required for the collisional excitation of CO.

The constant ratio $N(\text{H}_2)/W(\text{CO})$, now widely adopted to compute molecular masses from CO observations both in individual molecular clouds (e.g., Maddelena *et al.* 1986) and in external galaxies (reviewed by Morris and Rickard 1982), has recently been calibrated by comparison of CO, 21 cm, and γ -ray surveys over large regions of the Galaxy (Lebrun *et al.* 1983; Bloemen *et al.* 1984, 1986), the γ -ray intensity being assumed proportional to the total gas column density $[N(\text{H I}) + N(\text{H}_2)]$ and the 21 cm being used to determine $N(\text{H I})$. These studies put $N(\text{H}_2)/W(\text{CO})$ in the range $1\text{--}3 \times 10^{20} \text{ cm}^{-2} \text{ K}^{-1} \text{ km}^{-1} \text{ s}$; here we adopt 2×10^{20} , mainly for consistency with the parallel analysis by Myers *et al.* (1986; see Appendix B).

With this ratio and a mean molecular weight per H_2 molecule of $2.72m_{\text{H}}$ (Allen 1973), the mass of a complex can be expressed as

$$M = 1.3 \times 10^3 S D^2,$$

where M is in solar masses, D is the distance in kiloparsecs, and S the apparent CO luminosity of the complex (i.e., its total CO emission integrated over velocity and solid angle, in units of $\text{K km s}^{-1} \text{ deg}^2$). For the determination of S for each complex see § IIa and Appendix B, and for the resultant masses see Table 2.

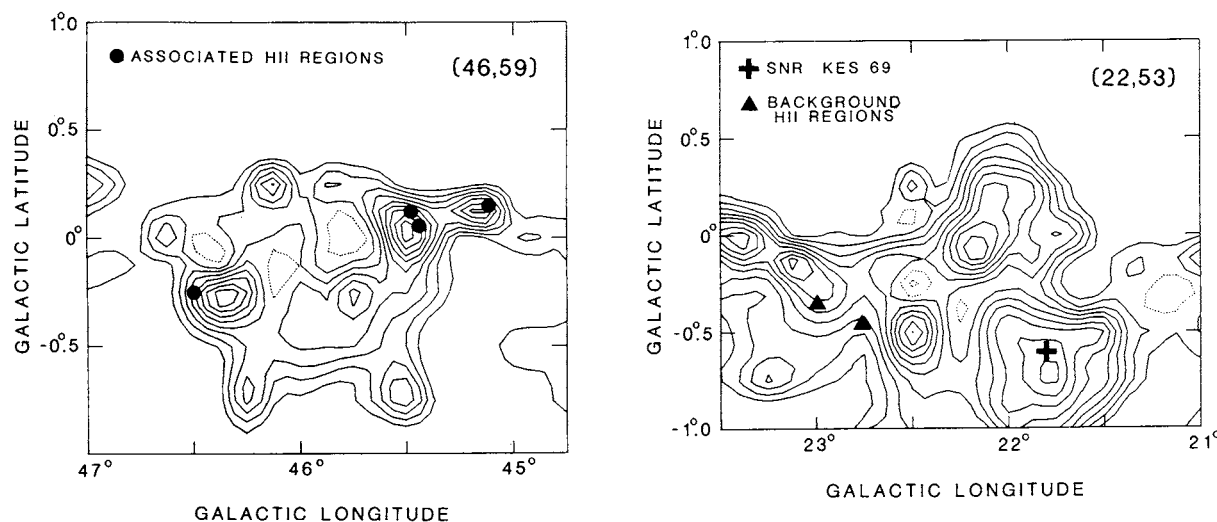


FIG. 5.—CO spatial maps of the large molecular complexes (a) [46,59] and (b) [22,53]. The contour interval in both maps is 5 K km s^{-1} . In (a) the emission is integrated over velocity from 50 to 65 km s^{-1} ; the dots mark the positions of H II regions with recombination-line velocities close to that of the complex. In (b) the emission is integrated from 40 to 60 km s^{-1} . The triangles mark the positions of H II regions with velocities of $\sim 75 \text{ km s}^{-1}$, much larger than that of the complex; these H II regions show H_2CO absorption at the velocity of the complex, suggesting the complex lies at the near kinematic distance. The cross marks the position of the SNR Kes 69; its estimated distance of 4.2 kpc agrees well with the near kinematic distance.

TABLE 2
THE BRIGHTEST CO SOURCES IN THE LONGITUDE-VELOCITY DIAGRAM

Designation (<i>l</i> , <i>v</i>) ^a	<i>l</i>	<i>b</i>	$\Delta v(\text{FWHM})$ (km s^{-1})	<i>D</i> (kpc)	Distance Source	<i>R</i> (pc)	$\log(M/M_{\odot})$
14,20	14.4	-0.4	10	2.3	b	53	6.05
14,39	14.2	-0.1	8	4.4	c	50	5.93
17,44	16.8	-0.2	9	4.4	d	56	6.03
17,22	16.8	+0.4	9	2.0	b	33	5.79
18,48	18.2	-0.3	7	4.4	c	48	6.03
19,65	18.8	-0.5	8	5.5	c	58	5.86
20,26	19.5	0.0	6	2.2	b	14	4.95
20,42	20.0	-0.7	10	3.8	c	35	5.46
22,53	22.1	-0.2	9	4.4	e	61	6.06
23,78N	23.0	-0.1	11	5.9	e	81	6.05
23,78F	23.0	-0.1	11	12.6	c	< 174	6.71
24,98	23.8	+0.1	15	7.1	c	116	6.46
25,55N	24.5	-0.2	12	4.2	d	66	6.12
25,55F	25.3	-0.5	13	13.9	c	97	6.68
29,80	28.8	-0.1	10	5.7	e	86	6.33
29,52	29.0	-0.7	4	3.8	e	12	5.00
31,95	30.5	0.0	18	6.9	c	113	6.50
31,48	31.0	0.0	11	13.7	c	123	6.45
35,44	35.0	-0.7	10	3.1	c	52	6.25
36,57	36.3	-0.1	11	12.1	c	107	6.63
37,82	33-39	~0.0	13	9.5	g	h	h
39,32	38.9	+0.4	8	2.2	d	37	5.76
39,42	39.0	-0.5	4	2.9	d	16	5.07
40,59	39.6	-0.3	11	11.2	c	105	6.37
41,37	41.1	0.0	6	2.6	d	31	5.82
42,63	41.9	-0.4	14	10.2	g	131	6.59
44,60	44.5	-0.2	12	9.6	c	74	5.87
46,59	45.9	-0.2	9	9.2	c	100	6.25
46,25	46.0	+0.2	3	1.8	d	12	4.71
49,59	49.5	-0.3	10	7.3	c	74	6.08
50,45	50.2	-0.5	8	3.6	d	35	5.40
52,59	52.1	-0.3	8	6.1	f	81	6.26
53,24	53.4	0.0	4	1.9	d	12	4.88
56,36	55.7	0.0	7	5.6	f	54	5.92

^a *l* is to the nearest degree; *v* is LSR radial velocity in km s^{-1} .

^b Spectroscopic parallax of associated optical cluster.

^c CO kinematic distance with ambiguity resolved by associated H II region.

^d Near kinematic distance indicated by the large latitude extent of the cloud.

^e Near kinematic distance indicated by H₂CO absorption at the cloud velocity in the continuum of an H II region lying between the cloud's near and far kinematic distances.

^f Velocity close to or greater than the terminal velocity, so assigned to the subcentral point.

^g Other; see Appendix A.

^h The mass for this feature, which corresponds to the Aquila Spur (see Appendix A), cannot be obtained by the method used for the other clouds, because the emission disappears after subtraction of the background model.

ii) Distance

Distances to most complexes were determined kinematically, using the rotation curve of Burton (1971). Various indirect methods, none entirely reliable, can be used to resolve the kinematic distance ambiguity for objects within the solar circle. Quite often a complex can be associated with one or more H II regions for which the distance ambiguity is resolved by atomic and molecular absorption measurements (see, e.g., Lockman 1979). In other instances, a complex can be assigned to the near distance because it produces H₂CO absorption against the continuum of one or more higher velocity H II regions, that is, those which must lie between the near and far distances of the complex. Yet another method to resolve the ambiguity is provided by the $R\text{-}\Delta V$ relation derived in § IIc. In principle, the observed line width and angular radius of the complex can be used with the $R\text{-}\Delta V$ relation to derive a distance directly; in practice, the scatter of the $R\text{-}\Delta V$ relation makes such a distance uncertain to roughly $\pm 50\%$, but on occasion the relation is still a useful tool for resolving the

distance ambiguity. This method is essentially a refinement of the classic use of angular size to discriminate between near and far distances (Schmidt 1957).

Generally, we applied one or more of these methods to each complex, and, when necessary, considered other data bearing on the distance (e.g., the $\Sigma\text{-}D$ distance of an associated SNR, apparent distance from the Galactic plane, or the absence of H₂CO absorption against the continuum of a higher velocity H II region). In three instances when spectroscopic distances of associated optical clusters were available, these were preferred to kinematic distances. Our distance determination for each complex is discussed in Appendix A, and the most reliable method of distance determination is listed in Table 2.

Two examples serve to illustrate the methods used to resolve the kinematic distance ambiguity (see Fig. 5). The complex [46,59] was assigned the far kinematic distance because of its apparent association with three H II regions that lie between $l = 45^\circ$ and $l = 45^\circ 5'$; these show H I absorption against their continuum emissions at velocities to 70 km s^{-1} (Downes *et al.*

1980) and were therefore assigned the far kinematic distance. The other complex, [22,53], was assigned the near kinematic distance for three reasons: First, and most important, Downes *et al.* observed H_2CO absorption features at the complex velocity against the continuum emissions of two H II regions (Fig. 5b) that have recombination line velocities ($\sim 75 \text{ km s}^{-1}$) larger than that of the complex ($\sim 53 \text{ km s}^{-1}$); the complex could produce the observed H_2CO absorption only if it is at the near kinematic distance. Second, the large angular size of this complex suggests the near kinematic distance, because at the far distance the complex would have an unacceptably large diameter—in excess of 350 pc. Third, the complex may be associated with the SNR Kes 69, which, from the Σ - D relation of Milne (1979), lies close to the near kinematic distance of the complex.

iii) Radius and Line Width

The angular areas of the complexes were measured from their spatial maps and converted to the actual projected areas A with the distances in Table 2; the effective radii (Table 2) are defined as $(A/\pi)^{1/2}$. The line widths were measured from composite line profiles of the complexes derived by averaging the spectra within a square region centered on the complex and equal on a side to its angular radius. These composite profiles often proved quite complicated, so the FWHM line widths (Table 2) were estimated from Gaussian profiles fitted by eye, rather than by a least-squares fit.

c) Statistical Cloud Properties

It is apparent to the eye in Figure 1 that the line widths of the Perseus arm clouds tend to increase with increasing cloud size. Investigation of this effect (Dame and Thaddeus 1982) showed that the increase can be approximated by a power-law relation between the line widths and the clouds' absolute CO luminosities. Recently, similar power-law relations between line width and radius have been determined from somewhat less homogeneous cloud samples by several groups (for a review, see Myers 1983). Our cloud sample (Table 2) provides a means to test and calibrate this relation over a large range of cloud sizes.

The good correlation between $\log R$ and $\log \Delta V$ evident in Figure 6 confirms the existence of a power-law relation between cloud line width and size and extends the relation to include complexes with masses up to 10 times those considered

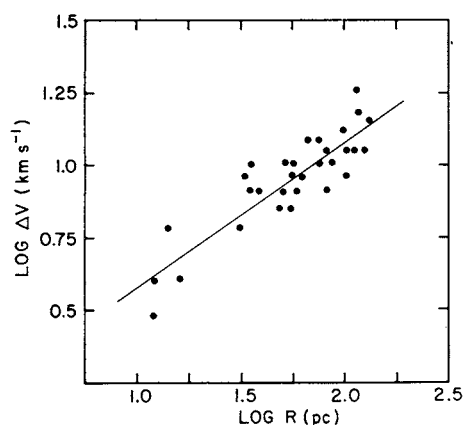


FIG. 6.—Logarithm of the observed line width ΔV (FWHM) of each complex in Table 2 vs. the logarithm of its radius R . The straight line is a least-squares fit given by the equation $\log \Delta V = 0.08 + 0.50 \log R$.

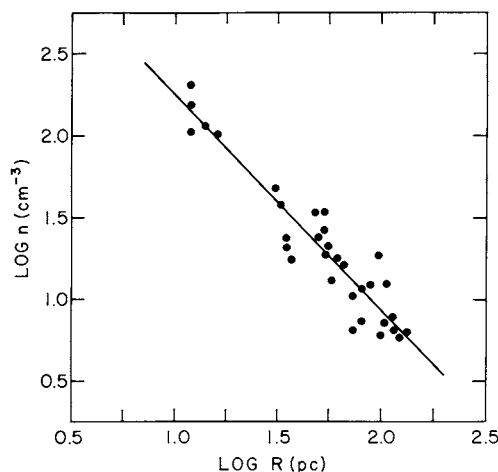


FIG. 7.—Logarithm of the mean H_2 density n of each complex in Table 2 vs. the logarithm of its radius R . The H_2 densities were computed directly from the masses and radii in Table 2, assuming spherical clouds and a mean molecular weight per H_2 molecule of $4.61 \times 10^{-24} \text{ g}$. The straight line is a least-squares fit given by the equation $\log n = 3.56 - 1.32 \log R$.

previously (e.g., by Larson 1981). The straight line is a least-squares fit given by the equation

$$\Delta V = AR^\alpha,$$

with $A = 1.20 \pm 0.22$ and $\alpha = 0.50 \pm 0.05$. Considering the irregular shapes and complicated line profiles of many of the complexes, the correlation is surprisingly good, with a linear correlation coefficient of 0.89. The power-law exponent is in excellent agreement with previous determinations (e.g., Larson 1981; Leung, Kutner, and Mead 1982; Myers 1983) and is consistent with a similar mass–line width relation derived from the Perseus arm (Fig. 1) by Dame and Thaddeus (1982).

The densities of the complexes decrease with increasing size (Fig. 7), as expected if gravitationally bound or nearly so. The straight line is a least-squares fit given by the equation

$$\langle n(\text{H}_2) \rangle = BR^{-\beta}. \quad (3)$$

With $n(\text{H}_2)$ in units of cm^{-3} and R in pc, $B = 3.6 \pm 1.2 \times 10^3$ and $\beta = 1.3 \pm 0.1$. Assuming a mean molecular weight per H_2 molecule of $2.72m_{\text{H}}$, the mean H_2 density $\langle n(\text{H}_2) \rangle$ was computed directly from the values of M and R given in Table 2. The power-law exponent β agrees with that found by Myers (1983) for dense molecular cores and is close to the value of 1.1 derived by Larson (1981) for clouds (and regions within clouds) that range in mass from $1 M_\odot$ to $3 \times 10^5 M_\odot$.

Most of the complexes appear to be in approximate virial equilibrium, as the power-law exponents $\alpha = 0.5$ and $\beta = 1.3$ determined above suggest. (For clouds in strict virial equilibrium, $\alpha + \beta/2 = 1$.) For a uniform, spherical cloud in virial equilibrium, the FWHM velocity dispersion of the internal motions that support it against gravitational collapse is given by

$$\Delta V_{\text{vt}} = \left(\frac{8G \ln 2}{5} \frac{M}{R} \right)^{1/2}, \quad (4)$$

where G is the gravitational constant, R the radius of the cloud, and M its mass. The internal motions, largely supersonic, probably include turbulence on many scales (Larson 1981), perhaps even the orbital motions of large clumps within the cloud. We assume that the net velocity dispersion of these

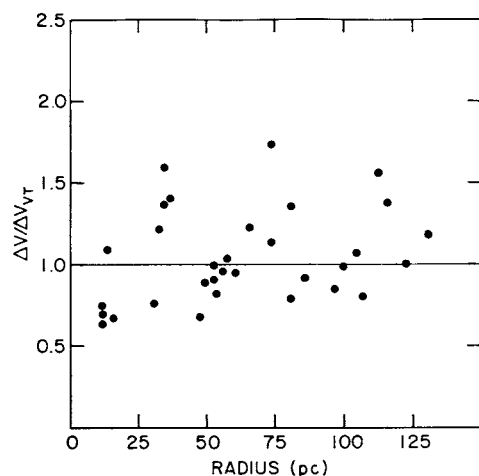


FIG. 8.—Ratio of the observed line widths ΔV (FWHM) to the virial-theorem line widths ΔV_{vir} (FWHM), computed from eq. (4), for the complexes in Table 2 and plotted as a function of their radii. The straight line is a least-squares fit given by the equation $\Delta V/\Delta V_{\text{vir}} = 0.89 + 0.002 R$ (pc).

motions is equal to the CO line width averaged over the entire cloud. The composite line widths ΔV (Table 2) are compared to the values expected in virial equilibrium ΔV_{vir} in Figure 8; the average ratio of $\Delta V/\Delta V_{\text{vir}}$ is 1.04 ± 0.29 . In view of the large systematic uncertainties in the cloud masses—arising about

equally from the background removal (Appendix B) and from the $N(\text{H}_2)/W(\text{CO})$ ratio (§ IIb) and amounting to nearly a factor of 2—this close agreement may be partially fortuitous. Nevertheless, the internal motions of the complexes appear at least partly governed by self-gravity, our data being consistent with rough virial equilibrium for most of the complexes.

III. GALACTIC DISTRIBUTION

The locations in the Galactic plane of all the complexes in our catalog (Table 2) with masses above $10^5 M_\odot$ are shown in Figure 9, where each complex is marked by a circle with a size proportional to the cube root of its mass. The Sagittarius logarithmic spiral is a least-squares fit to the 17 complexes that trace the arm. Since the complexes do not as clearly delineate the innermost spiral arms, the Scutum and 4 kpc spirals were, rather than fitted, taken directly from an analysis of inner galaxy 21 cm emission by Shane (1972).

The largest complexes delineate the Sagittarius arm with remarkable clarity over more than 120° of galactocentric azimuth (Fig. 9). The 17 large complexes we identified in the arm have a total mass of $28 \times 10^6 M_\odot$ and an average spacing of ~ 1 kpc, comparable to the spacing of the regular strings of H II regions observed in many external spirals (see, e.g., Elmegreen and Elmegreen 1983). The overall spiral pattern of one or possibly two closely spaced arms interior to the more extended Sagittarius arm is similar to that derived in numerous previous

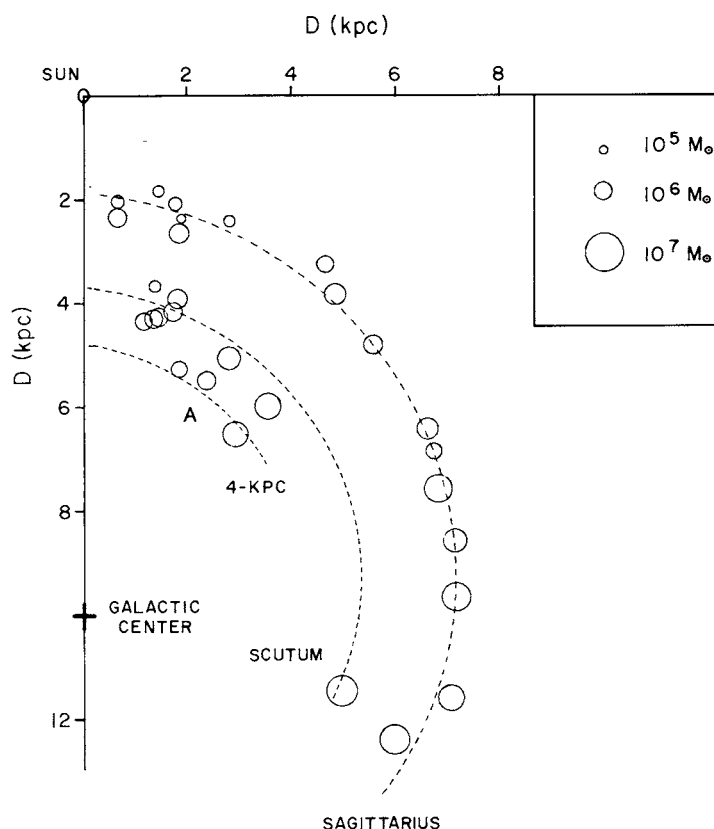


FIG. 9.—The locations in the Galactic plane of the large complexes listed in Table 2; the four clouds with masses less than $10^5 M_\odot$ are not shown. The circle sizes are proportional to the cube roots of the cloud masses. For A, see § III.

The Sagittarius spiral, an unweighted least-squares fit to the positions of the 17 complexes that outline the arm, has a pitch angle of $5^\circ.3$ and crosses the Sun-center line at $R = 8.24$ kpc. The Scutum and 4 kpc spirals were not fitted through the clouds but taken directly from the 21 cm analysis of the inner Galaxy by Shane (1972). The Scutum spiral has a pitch angle of 7° and crosses the Sun-center line at $R = 6.39$ kpc; the 4 kpc spiral has a pitch angle of 10° and crosses the Sun-center line at $R = 5.28$ kpc.

Population I studies (e.g., Burton and Shane 1970 and Shane 1972, using H I; Georgelin and Georgelin 1976 and Downes *et al.* 1980, using H II regions).

A surprising feature that emerges in Figure 9 is an asymmetry in the distribution of large complexes in the inner Galaxy. Most of the complexes between 4 and 7 kpc from the Galactic center appear to lie at the near kinematic distance (the cluster of objects near *A* in the figure), indicative perhaps of a large-scale bar in the distribution of clouds. Even though complexes on the far side of the Galaxy are difficult to identify and some, undoubtedly, have been missed (see § IV and Appendix C), the clarity of the Sagittarius arm to a distance of 14 kpc suggests that difficulties in detection may not entirely explain the asymmetry. Bok's "Finger of God" in the early 21 cm versions of Figure 9, pointing to the observer and telling him his reconstruction of the Galaxy is seriously biased, is also not apparent. Similar asymmetries have been deduced from previous studies: Georgelin and Georgelin (1976) of H II regions, Shane (1972) of 21 cm emission, and Bania (1980) of CO emission. If such an asymmetry actually exists, then the CO luminosity and, consequently, the molecular mass of the inner Galaxy have been overestimated by the models of Cohen and Thaddeus (1977) and Sanders, Solomon, and Scoville (1984), which assume that the inner Galaxy emission is axially symmetric about the Galactic center.

The clipped spatial maps (see § IIa) shown in Figure 10 provide a panoramic view of all of the complexes: Figure 10a shows the complexes in the Sagittarius arm, and Figure 10b shows those in the region of the Scutum and 4 kpc arms. The inserts, essentially a perspective view of Figure 9, plot the Galactic distribution of the complexes viewed from the perspective of an observer located 2 kpc above the Sun.

The fairly regular spacing of the complexes in the Sagittarius arm is clearly seen in Figure 10a. The massive complexes in the near side of the arm—M17, M16, and W44—have larger angular sizes and are more widely separated in longitude than similar complexes in the far side of the arm. The thickness in latitude of the complexes in the far side tends to decrease with increasing distance from the Sun (i.e., with decreasing longitude), but the map also shows one exception to this tendency, the emission near $l = 35^\circ$, which probably arises from high-velocity gas associated with the very large near complex [35,44] apparently associated with the SNR W44 (Dame 1983). Unlike the complexes in the Sagittarius arm, those in the inner Galaxy, as seen in Figure 10b, appear densely packed and irregularly positioned; in addition, the background emission is stronger, especially, as expected, in the highest velocity map (*top*) of the region of strong velocity crowding near the terminal velocity.

Although our sample of large complexes is not complete, being biased against distant clouds (see § IV), it is not biased against clouds in the interarm regions. On the contrary, individual complexes should be more easily distinguished in the interarm regions, where the background level is lower. Since a very large fraction of our sample of large complexes lie in the spiral arms, it is likely that a similar fraction of all large clouds lie in the arms.

The general confinement of the largest complexes to spiral arms implies that most of the molecular mass is in the arms, numerous investigations of the molecular cloud mass spectrum (see Appendix C and references therein) having already shown that most of the molecular gas is in the larger clouds. Whether smaller clouds in the inner Galaxy are similarly contained in

the arms remains very difficult to determine, but, in any case, despite their large number, these clouds contain little of the total molecular mass. As first noted by Cohen *et al.* (1980), the nearly empty lane between the Perseus and Local arms apparent in Figure 1 suggests that the smaller clouds follow the large clouds and also have a high arm-interarm contrast.

The clarity of the Sagittarius arm in our maps (Figs. 9 and 10a) suggests that a more comprehensive inventory of such complexes would produce a clear picture of the overall spiral structure. Indeed, CO data from the fourth Galactic quadrant (Cohen *et al.* 1985) reveals that the Carina arm is at least as clearly delineated by large molecular complexes as the Sagittarius arm is and may represent the extension of the Sagittarius arm into the fourth quadrant.

IV. COMPLETENESS OF THE CLOUD SAMPLE

Table 2, which is a list of the *brightest* CO sources in our survey, is neither a complete nor an unbiased sample of large molecular clouds in the first quadrant. Rather, as we show below, the total number of clouds and the mass distribution in this table are roughly what would be expected for an apparent-luminosity-limited sample of molecular clouds in the inner Galaxy. Such a sample is of course biased toward, and is most nearly complete for, the very largest complexes, but it also contains some small clouds that happen to lie close to the Sun. A list of the largest molecular complexes can be distilled from Table 2, once distances and masses are determined.

The total number and the mass distribution expected for an apparent-luminosity-limited sample of clouds are readily calculated from the known mass spectrum and total mass of molecular clouds in the inner Galaxy, given an appropriate value for the apparent-luminosity cutoff (S_{\min} , in units of $\text{K km s}^{-1} \text{ deg}^2$). Here, S_{\min} is the minimum apparent CO luminosity a cloud must have to be included in our sample; it is determined less by instrumental noise than by source confusion, the complexity of the overall emission: only the brightest sources in the jumble of inner Galaxy CO emission are recognized as individual clouds in our analysis. In Appendix C we show that S_{\min} appears to differ for the inner and the outer Galaxy; we estimate upper and lower limits for both regions and use these to calculate the results shown in Table 3, where N_{tot} is the total number of clouds within the solar circle in each half-decade interval of mass, calculated from the known mass spectrum and total molecular mass of the inner Galaxy; N_{acc} , the number of such clouds lying between $l = 12^\circ$ and $l = 60^\circ$; N_{exp} , the number of accessible clouds we expect to detect (those bright enough that $S > S_{\min}$); and N_{obs} , the number actually observed.

TABLE 3
PREDICTED AND OBSERVED MASS DISTRIBUTIONS
OF CLOUD SAMPLE

$\log(M/M_\odot)$	N_{tot}^a	N_{acc}^b	N_{exp}^c	N_{obs}^d
4.24–4.75.....	1088	392	1–2	1
4.75–5.25.....	648	233	2–4	4
5.25–5.75.....	386	139	6–8	4
5.75–6.25.....	230	83	9–14	12
6.25–6.75.....	126	45	17–27	12

^a Total number within the solar circle.

^b Number accessible to our survey (i.e., within $l = 12^\circ$ – 60°).

^c Number of accessible clouds near enough to detect (using lower and upper limits for the luminosity cutoff S_{\min}).

^d Number observed.

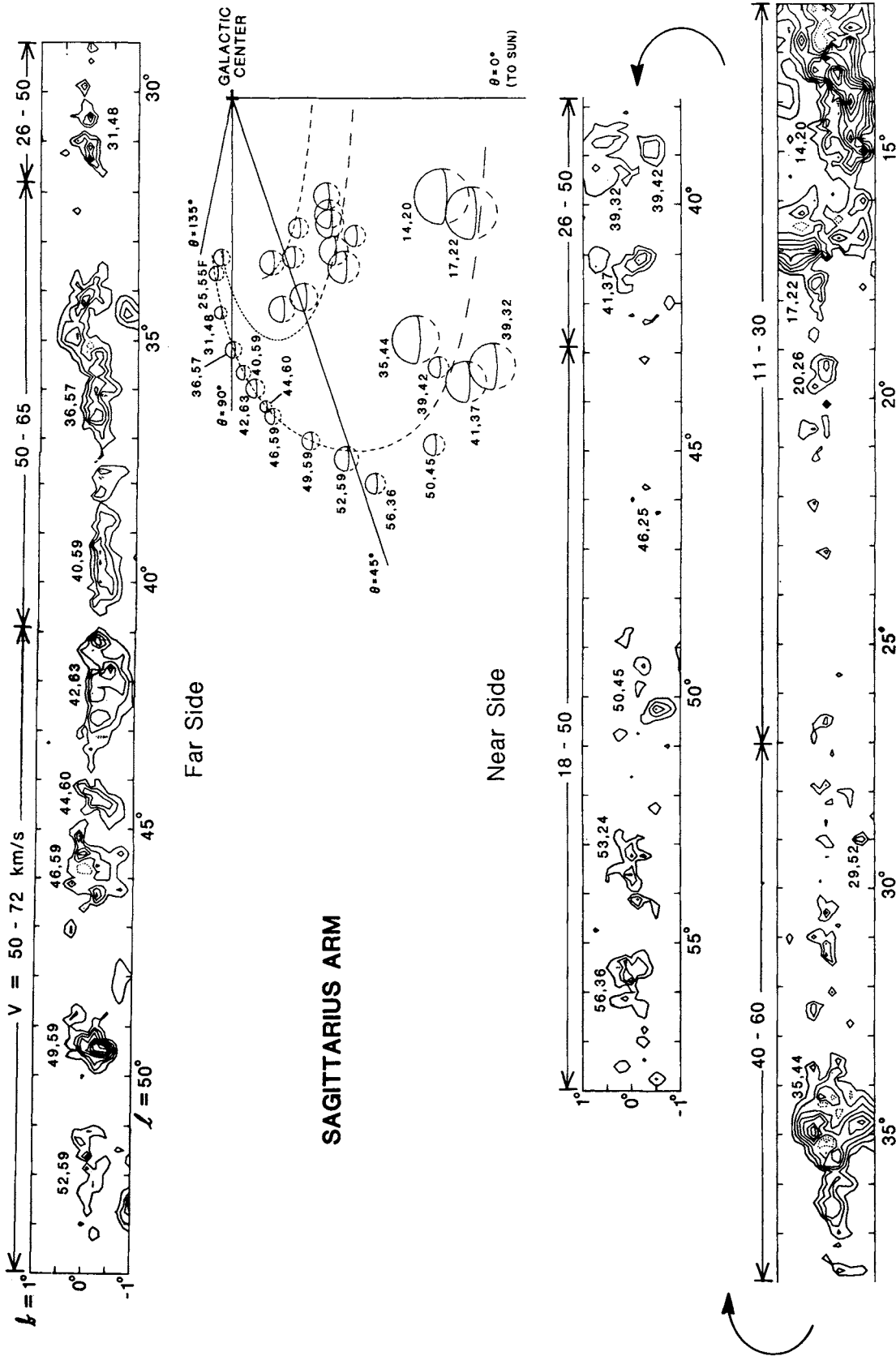


FIG. 10a

FIG. 10.—Spatial maps of the molecular clouds discussed in the text and listed in Table 2. Clouds in (a) the Sagittarius arm; (b) the Scutum and 4 kpc arms. The maps were produced by setting all spectral channels with $T < 2$ K to zero before integrating over velocity. The velocity integration limits change by discrete steps along the maps, in (a) to follow the velocity of the Sagittarius arm and in (b) simply to distinguish individual complexes in the crowded inner Galaxy. In every map the contour interval is 9.8 K km s^{-1} . The figures between the maps show the distribution of the clouds in the Galactic plane viewed from the perspective of an observer located 2 kpc above the Sun. The circle diameters are proportional to the cube roots of the cloud masses and to the inverses of the cloud distances, and all the clouds are assumed to lie in the Galactic plane. Straight lines from the Galactic center at galactocentric longitudes of 0° , 45° , 90° , and 135° are shown in perspective. The four clouds with masses less than $10^5 M_\odot$ which are not shown in the figure appear labeled in the spatial maps. The dotted curves are logarithmic spirals shown in perspective; the parameters of the spirals are the same as in Fig. 9.

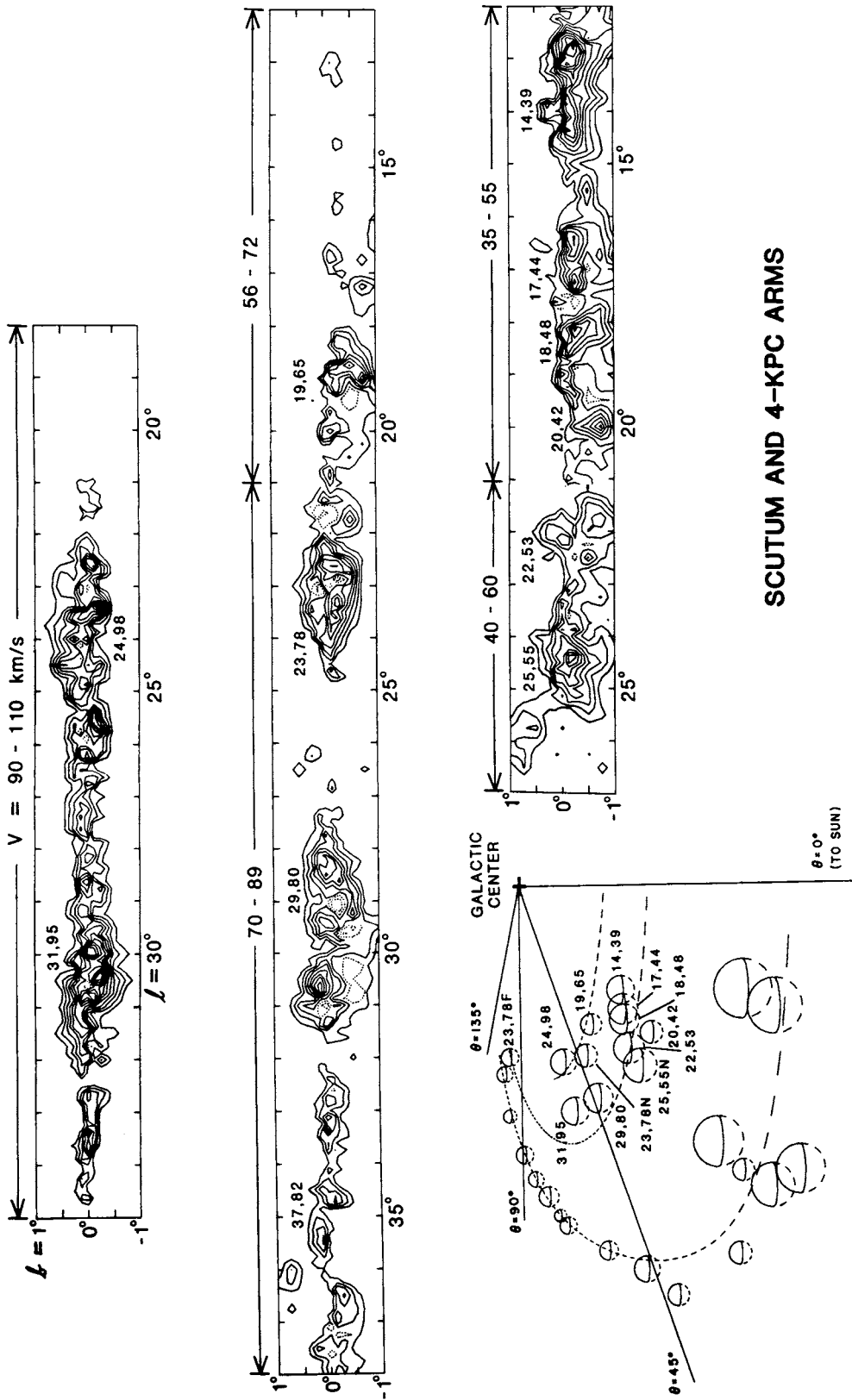


FIG. 10b

The good agreement between the expected and observed numbers in Table 3 supports our contention that our cloud sample constitutes an approximate apparent-luminosity-limited sample of inner Galaxy molecular clouds. As expected, our sample contains fewer small clouds than large, opposite to what would be expected for an unbiased or a mass-limited sample. In view of the large uncertainty and variability of the apparent-luminosity cutoff S_{\min} (see Appendix C), the discrepancy between N_{\exp} and N_{obs} in the highest mass bin is probably not significant; further, this bin is sensitive to the precise behavior of the inner Galaxy mass spectrum at the high-mass end, which is not well known.

The completeness of our cloud sample can be gauged by a comparison of the number of observed clouds, N_{obs} , and the calculated number of accessible clouds, N_{acc} , given in Table 3 as a function of cloud mass. Not surprisingly, we detect only a tiny fraction of the low-mass clouds and relatively larger fractions of the more massive clouds which are detectable over larger areas. We suspect that in reality a larger fraction of the most massive clouds have been detected, and that fewer such clouds are accessible than are estimated in Table 3. In the Sagittarius arm, for example (see Fig. 10a) it is unlikely that any clouds comparable in size to the largest we identify there could have escaped detection. Those that may have escaped detection must lie either very far away or in the confusion of the molecular ring region. Our estimates of the numbers of accessible clouds depend on the total mass and the mass spectrum of inner Galaxy clouds; we have already suggested (§ III) that the total mass might be overestimated, and our mass spectrum, particularly at the high-mass end, is even more likely to be in error, since it was determined mainly from rather small clouds in the outer Galaxy. Either a smaller total mass or a shallower mass spectrum, with more small clouds and fewer large ones, would reduce the difference between N_{acc} and N_{obs} in the high-mass bins.

In our judgment it is unlikely that our list of the largest complexes ($M > 5 \times 10^5 M_{\odot}$) could be greatly expanded even with a fully sampled survey of much higher sensitivity and angular resolution than our own. The basic noise obscuring these large clouds is not instrumental noise but the confusion of the overall emission produced by clouds of all sizes. An isolated cloud of just a few times $10^5 M_{\odot}$ could readily be seen by our survey to well over 20 kpc, but in the inner Galaxy, where clouds are crowded both spatially and in velocity, such a cloud would be difficult to identify as a discrete object.

V. CONCLUSION

After identifying and defining the most prominent CO sources in the first Galactic quadrant, we found that many of

them correspond to very large molecular cloud complexes similar to the one associated with NGC 7538 in the Perseus arm. The largest, with masses greater than $10^6 M_{\odot}$ and diameters over 100 pc, are an order of magnitude more massive than a standard giant molecular cloud such as that toward the Orion Nebula (Kutner *et al.* 1977). Because these complexes contain a substantial fraction of the total Galactic CO luminosity and are among the best defined molecular clouds, they can easily be identified to large distances in the Galaxy and, with the aid of various associated Population I objects, can be located in the Galactic plane.

The location of these largest complexes in the Galactic plane reveals a pattern of spiral arms similar to that found by previous 21 cm and H II region studies: an extended Sagittarius arm with one or, possibly, two closely spaced arms interior to it. The location of the complexes within the spiral arms supports the conclusion of Cohen *et al.* (1980) that the apparent spiral features in the CO longitude-velocity diagram are due to the existence of genuine molecular arms, rather than, as Liszt and Burton (1981) maintain, to large-scale streaming motions. The containment of the largest complexes in the arms also demonstrates that CO emission is enhanced in the arms not merely because the clouds there are hotter (Sanders, Scoville, and Solomon 1985) but mainly because they are larger and more massive. The similarly regular spacing of the large complexes in the Sagittarius arm and of the giant H II regions, the classic "beads on a string" that trace the arms of external galaxies, suggests that the regularity of molecular complexes is the underlying cause of the regularity of their optically more prominent offspring, the giant H II regions.

Most of the complexes identified interior to the Sagittarius arm lie at the near kinematic distance, suggesting a large-scale departure from axial symmetry with respect to the Galactic center in this region. Although possibly due to the incompleteness of our cloud sample at large distances, this asymmetry, if real, may have important implications for the radio, infrared, and γ -ray studies of the inner Galaxy that assume axial symmetry about the Galactic center.

Several of these complexes (e.g., M17, W44, and W51) have been thoroughly studied; many others (Table 2) clearly merit detailed study. A more comprehensive inventory of them will lead to a better understanding of the life cycle of molecular clouds and provide a clearer picture of the Galactic spiral structure.

We thank P. C. Myers for helpful discussions, E. S. Palmer for help operating and maintaining the 1.2 m telescope, A. Smith for assistance with data analysis, E. Sarot for editorial assistance, and E. Michaud for typing the manuscript.

APPENDIX A

DISCUSSION OF INDIVIDUAL CLOUDS

Here we describe how we determined the distance to each complex and comment, where necessary, on definition, mass, and peculiar cloud properties. Associated H II regions, identified by their Galactic longitudes, are labeled "near" or "far" when known to lie at either the near or the far kinematic distance. The frequently cited H II region catalogs of Downes *et al.* (1980) and Georgelin and Georgelin (1976) are abbreviated as DWBW and GG; and the low angular resolution (1°) CO survey of Dame and Thaddeus (1985), covering roughly $b = -4^\circ$ to $b = +6^\circ$ from $l = 12^\circ$ to $l = 100^\circ$, will be referred to as the Columbia wide latitude survey.

[14,20], M17.—This cloud, visible as a dark nebula, is clearly associated with the H II region M17. We adopt the spectroscopic distance to M17 derived by Crampton, Georgelin, and Georgelin (1978).

[14,39].—Assignment of the near kinematic distance is based on the proximity of the cloud to three “near” H II regions at $l = 13^{\circ}998$, $14^{\circ}600$, and $14^{\circ}626$ (DWBW). The low-longitude edge of the cloud was taken to be $13^{\circ}5$; the emission below this longitude appears to be associated with another cloud near W33 with a much larger velocity extent, which, because its emission extends outside the longitude range of our survey, is not included in our catalog (Table 2). Although in the highly smoothed (l, v)-diagram (Fig. 2) the longitude extent of cloud [14,39] is ambiguous, the cloud appears as a well-defined feature at higher resolution (see Fig. 3 or 4).

[17,44].—Assignment of the near kinematic distance is based on the large angular size and small velocity extent of the cloud. At the far distance, this object would have an unacceptably large radius of 187 pc (larger than any cloud in our catalog) and would extend more than 130 pc below the plane.

[17,22], M16.—The spectroscopic distance to the associated stellar cluster NGC 6611 is adopted (GG No. 9). The Columbia wide latitude survey shows emission from this object lying outside the latitude range of the present survey. Based on these additional data, the cloud mass was increased by 63%.

[18,48].—Assignment of the near kinematic distance is based on the proximity of the cloud to the “near” H II regions at $l = 18^{\circ}143$, $18^{\circ}185$, $18^{\circ}231$, and $18^{\circ}258$ (DWBW) and on the optical H II region GG No. 10.

[19,65], W39.—Assignment of the near kinematic distance is based on proximity of the cloud to the “near” H II regions at $l = 18^{\circ}881$, $18^{\circ}936$, $19^{\circ}066$, and $19^{\circ}614$ (DWBW).

[20,26].—The spectroscopic distance to a presumably associated star cluster (GG No. 11) lying close to the near kinematic distance of the cloud is adopted; a “near” H II region exists in the vicinity of the cloud at $l = 20^{\circ}988$ (DWBW), and in the continuum of another H II region at $l = 18^{\circ}936$ (DWBW) the cloud is seen as an H₂CO absorption feature at 25.5 km s^{-1} . This cloud may be associated with the M16-M17 complex (clouds [14,20] and [17,22]) at approximately the same distance.

[20,42].—Assignment of the near kinematic distance is based on the proximity of the cloud to the H II regions at $l = 19^{\circ}608$ and $20^{\circ}074$ (DWBW). Its latitude, $-0^{\circ}75$, suggests it lies at the near distance; at the far distance, 15 kpc, its center would be rather far below the Galactic plane, about 200 pc.

[22,53].—This object is seen as an H₂CO absorption feature at velocities near 55 km s^{-1} in the continua of H II regions at $l = 22^{\circ}982$ and $22^{\circ}760$ (DWBW). Since the far kinematic distances of these H II regions are smaller than the far kinematic distance of the cloud, the cloud must lie at the near distance. Also, at the far distance the cloud radius would be abnormally large, about 200 pc. The cloud may be associated with the supernova remnant Kes 69 (at $l = 21^{\circ}8$, $b = -0^{\circ}6$); the surface brightness–diameter relation of Milne (1979) yields a distance of 4.2 kpc for the remnant, in good agreement with the near kinematic distance of the cloud of 4.4 kpc.

[23,78N] and [23,78F], W41.—This feature probably is a blend of two large clouds, one at the near kinematic distance [23,78N], the other at the far [23,78F]. A large number of “far” H II regions (e.g., at $l = 22^{\circ}760$, $22^{\circ}947$, $22^{\circ}982$, and $23^{\circ}254$ [DWBW]) coincide in direction and velocity with the feature, suggesting that at the far distance a very massive and active star-forming cloud exists. But at the far distance of 12.6 kpc, the cloud would have an unacceptably large diameter of ~ 350 pc. A strong H₂CO absorption feature at 81 km s^{-1} in the continuum of the H II region at $l = 23^{\circ}421$ (DWBW) lying near the subcentral point also argues for the existence of a fairly massive cloud at the near distance. The large angular size and strong H₂CO absorption associated with this near feature and the large number of H II regions associated with the far feature suggest that both components are massive, so we assume the emission is divided equally between the two. A blend of near and far clouds might be expected in this region, the intersection in (l, v)-space of the near side of the 4 kpc arm and the far side of the Scutum arm (Cohen *et al.* 1980).

[24,98].—Assignment of the near kinematic distance is based on the proximity of the cloud to the “near” H II region at $l = 23^{\circ}43$ (Lockman 1979; also GG). A large number of H II regions lie in the direction of this feature, all too close to the terminal velocity for distances to be resolved; the feature may result from several clouds spread along the tangent region of the 4 kpc arm.

[25,55N] and [25,55F].—This feature probably is a blend of two clouds, one at the near kinematic distance [25,55N], the other at the far [25,55F]. Although in a spatial map integrated over the full velocity range of the feature the far component is not obvious, in a more restricted velocity range surrounding the velocity of the “far” H II region W42 (at $l = 25^{\circ}382$ [DWBW]) it appears clearly. The far component coincides in direction and velocity with the “far” H II region W42. Its total CO luminosity was taken to be the integrated emission in the region $l = 25^{\circ}-25^{\circ}5$, $b = 0^{\circ}875-0^{\circ}125$, and $v = 50-62 \text{ km s}^{-1}$. Based on its latitude extent, the rest of the emission ($\sim 75\%$) was placed at the near distance, because at the far it would have an excessively large average diameter, over 400 pc.

For feature [25,55], as for feature [23,78], a blend of near and far clouds might be expected, because it lies near the intersection in (l, v)-space of the near side of the Scutum arm and the far side of the Sagittarius arm (Cohen *et al.* 1980).

[29,80].—Although this large complex is unusual in lacking associated H II regions, there are many H II regions in the same direction near the subcentral point, and this cloud is seen in absorption against four of them. The best examples are the H II regions at $l = 28^{\circ}658$ and $28^{\circ}801$ (DWBW), with H₂CO absorption features at 82.0 and 79.5 km s^{-1} respectively; the cloud must therefore be at the near distance.

[29,52].—An H₂CO absorption feature with the same velocity as the cloud is present in the continuum of the H II region at $l = 29^{\circ}944$ (DWBW) lying near the subcentral point, so the cloud must lie at the near distance. The mean latitude ($-0^{\circ}75$) also argues for the near distance, because at the far distance the cloud would lie about 190 pc below the plane.

[31,95].—Assignment of the near kinematic distance is based on H₂CO absorption at the velocity of the cloud in the continuum of the H II regions at $l = 30^{\circ}602$ and $31^{\circ}411$ and on the proximity of the cloud to the “near” H II regions at $l = 30^{\circ}776$ and $31^{\circ}401$ (DWBW). Although many H II regions exist in the direction of this feature, most are too close to the terminal velocity for their distances to be resolved, so the feature may result from several clouds spread along the tangent region of the Scutum arm.

[31,48].—Assignment of the far kinematic distance is based on the proximity of the cloud to the H II region at $l = 30^{\circ}539$ (DWBW). Its large velocity extent and location precisely in the plane (see Fig. 10a) also argue for the far distance.

[35,44], W44.—Assignment of the near distance is based on the proximity of the cloud to the H II regions at $l = 34^{\circ}254, 35^{\circ}063, 35^{\circ}194, 35^{\circ}346, 35^{\circ}603$, and $35^{\circ}663$ (DWBW). Its mass may be overestimated by as much as 50%, depending on what fraction of the emission in the range $v = 50\text{--}65 \text{ km s}^{-1}$ is associated with the cloud (for detailed discussion, see Dame 1983). To account for emission lying outside the latitude range of the present survey, the mass has been increased by 24%, based on data from the Columbia wide latitude survey.

[36,57].—Assignment of the far kinematic distance is based on the proximity of the cloud to H II regions at $l = 37^{\circ}439$ and $37^{\circ}538$ (DWBW) which coincide with the cloud in latitude and velocity and lie at its extreme high-longitude edge. The “near” H II region at $l = 36^{\circ}4, v = 57.4 \text{ km s}^{-1}$, a Sharpless object (S72) listed in the catalog of GG, lies almost 3° below the plane and so is probably not associated with this cloud. Although in the smoothed (l, v) -map (Fig. 2) the cloud is strongly blended with the W44 complex [35,44], it appears as a well-defined feature in the unsmoothed data (e.g., Fig. 4), and its much smaller latitude extent (Fig. 10a) further distinguishes it from W44. If some of the emission at $l < 36^{\circ}$ is associated with this cloud, its mass may be underestimated here.

[37,82].—This feature is distinguished from the others identified in Figure 2b by its long, filamentary appearance on the plane of the sky (Fig. 10b) and its disappearance on background subtraction (Appendix B). An interarm spur at this location has long been postulated by 21 cm observers (Weaver 1970; Shane 1972); this feature is apparently its molecular counterpart. It is discussed in detail in Dame (1983), where it is called the Aquila Spur. Assignment of the far kinematic distance is based on the assumption that the object is a small spiral spur, in which case its location and orientation in the (l, v) -plane are best modeled as a segment of the far side of a spiral arm. The object's small latitude extent also argues for the far distance.

[39,32].—In the Columbia wide latitude survey this cloud extends above $+3^{\circ}$ in latitude, so it must lie at the near distance; it may be associated with the nearby cloud [41,37] which has a similar latitude extent. To account for emission lying outside the latitude range of the present survey, the cloud mass has been increased by a factor of 2.3, based on data from the Columbia wide latitude survey.

[39,42].—This cloud appears small in the “clipped” spatial map (Fig. 10a) because it is a weak, extended feature, but in the unclipped data its latitude extent is $\sim 1^{\circ}$, corresponding to a linear size of $\sim 200 \text{ pc}$ at the far distance. Its latitude extent, rather large displacement from the plane ($\sim 0^{\circ}.5$), and small velocity extent all indicate it is near. It may be associated with the larger clouds [39,32] and [41,37] lying at about the same distance.

[40,59].—Assignment of the far kinematic distance is based on the proximity of the cloud to the “far” H II regions at $l = 37^{\circ}763$ and $37^{\circ}871$ (DWBW). These H II regions coincide with the complex in latitude and velocity but are somewhat displaced in longitude. The cloud has roughly the same latitude extent and negative displacement from the plane as the far-side clouds on either side, [36,57] and [42,63].

[41,37].—In the Columbia wide latitude survey this cloud extends above $+3^{\circ}$ in latitude, so it must lie at the near distance; it may be associated with the nearby cloud [39,32], which has a similar latitude extent. To account for emission lying outside the latitude range of the present survey, the cloud mass has been increased by 64%, based on data from the Columbia wide latitude survey.

[42,63].—The distance to this cloud is uncertain. Based on the similarity of this cloud in the spatial map (Fig. 10a) to the far clouds [44,60] and [46,59], it is assigned to the far distance. All three of these clouds have about the same latitude extent and negative displacement from the plane. That the cloud does not appear as an H_2CO absorption feature in the continuum of the H II region at $l = 42^{\circ}108$ (DWBW) argues weakly for the far distance, because the near and far kinematic distances of the H II region lie between the near and far distances of the cloud.

[44,60].—Assignment of the far kinematic distance is based on the proximity of the cloud to the H II region at $l = 45^{\circ}125$ (DWBW) at the cloud's high-longitude edge. The cloud is similar to the far-side cloud [46,59] in angular size, velocity extent, mean latitude, and apparent brightness.

[46,59].—Assignment of the far kinematic distance is based on the proximity of the cloud to the H II regions at $l = 45^{\circ}125, 45^{\circ}451$, and $45^{\circ}475$ (DWBW). (Some disagreement exists about the kinematic distance of the H II region at $l = 45^{\circ}451$: Lockman 1979 placed it at the near distance because higher velocity absorption features then seemed lacking, but DWBW cite H I absorption at velocities up to 70 km s^{-1} as evidence for the far distance.) A very weak “near” H II region in the vicinity of this cloud ($l = 46^{\circ}50$ from Lockman 1979) was assigned the near distance by Lockman (1979), based merely on a lack of high-velocity OH absorption; on the basis of existing data, DWBW considered the distance to this H II region unresolvable.

[46,25].—This cloud appears small on the “clipped” spatial map (Fig. 10a) because it is a weak, extended feature, but in the unclipped data its latitude extent is at least $1^{\circ}.5$, corresponding to a linear size of over 300 pc at the far distance. Its large latitude extent and small velocity extent both argue for the near distance. It may produce the H_2CO absorption feature at 24.8 km s^{-1} seen against the H II region at $l = 45^{\circ}125$ (DWBW).

[49,59], W51.—Assignment of the far kinematic distance is based on the proximity of the cloud to the H II regions at $l = 49^{\circ}384, 49^{\circ}437$, and $49^{\circ}486$ (DWBW); these H II regions and the cloud itself have been extensively studied (see, e.g., Mufson and Liszt 1979). Also of note are the VLBI measurements of relative proper motions of H_2O maser features in this source (Genzel *et al.* 1981) which yield a distance of $7 \pm 1.5 \text{ kpc}$, consistent with the far kinematic distance.

[50,45].—The distance to this object is uncertain. It is assigned the far distance based on its proximity to the “far” H II region at $l = 49^{\circ}407$ (DWBW), but this H II region may actually be associated with the W51 complex [49,59].

[52,59].—Its velocity being greater than the terminal velocity, this object was placed at the subcentral point, where it marks the tangent point of the Sagittarius arm.

[53,24].—Assignment of the near kinematic distance is based on the large angular size and small velocity extent of the cloud. This is a weak feature with a latitude extent in the “unclipped” data in excess of 2° , corresponding to a linear size at the far distance of over 300 pc .

[56,36].—Because its distance ambiguity could not be resolved and it lies less than 10 km s^{-1} from the terminal velocity, this cloud has been placed at the subcentral point. The distance, then, is quite uncertain, lying in the range $3\text{--}8 \text{ kpc}$.

APPENDIX B

REMOVING THE BACKGROUND OF SMALLER CLOUDS

The first step toward determining the masses of the complexes, many immersed in an extended background of emission, is to select an appropriate method for determining integrated CO intensities. Clipping at a fixed threshold (described in § II), one method of suppressing extended background emission, was used by Myers *et al.* (1986) to determine masses for a cloud sample that includes as a large subset all the complexes considered here. As the spatial maps in Figures 5 and 10 show, clipping effectively distinguishes large complexes from the background, but it does not take into account the variations of the background expected with varying longitude and velocity (e.g., the increase toward the terminal velocity and in the molecular ring region). Differing fundamentally from clipping, the approach adopted here is subtraction of a model background from the (l, v) -diagram.

For simplicity, we assumed that the background emission is symmetric about the Galactic center and that it has the same radial distribution as the overall CO emission; we used an analytic approximation of the overall CO radial distribution that Dame (1983) determined from the model of Cohen and Thaddeus (1977). Further, we assumed that the emission both is optically thin and has a one-dimensional velocity dispersion of 8 km s^{-1} , the value derived for low-mass ($< 10^4 M_\odot$) clouds by Stark (1979). With these simple assumptions, a model longitude-velocity diagram of the background emission was constructed and subtracted from the observed diagram (Fig. 3); the residual diagram is shown in Figure 11. The level of the background in this model was adjusted to remove as much intercloud emission as possible while leaving the large complexes intact. At the adopted background level, 63% of the nonlocal ($v > 20 \text{ km s}^{-1}$) emission in the observed diagram (Fig. 3) was removed for Figure 11, where the complexes appear

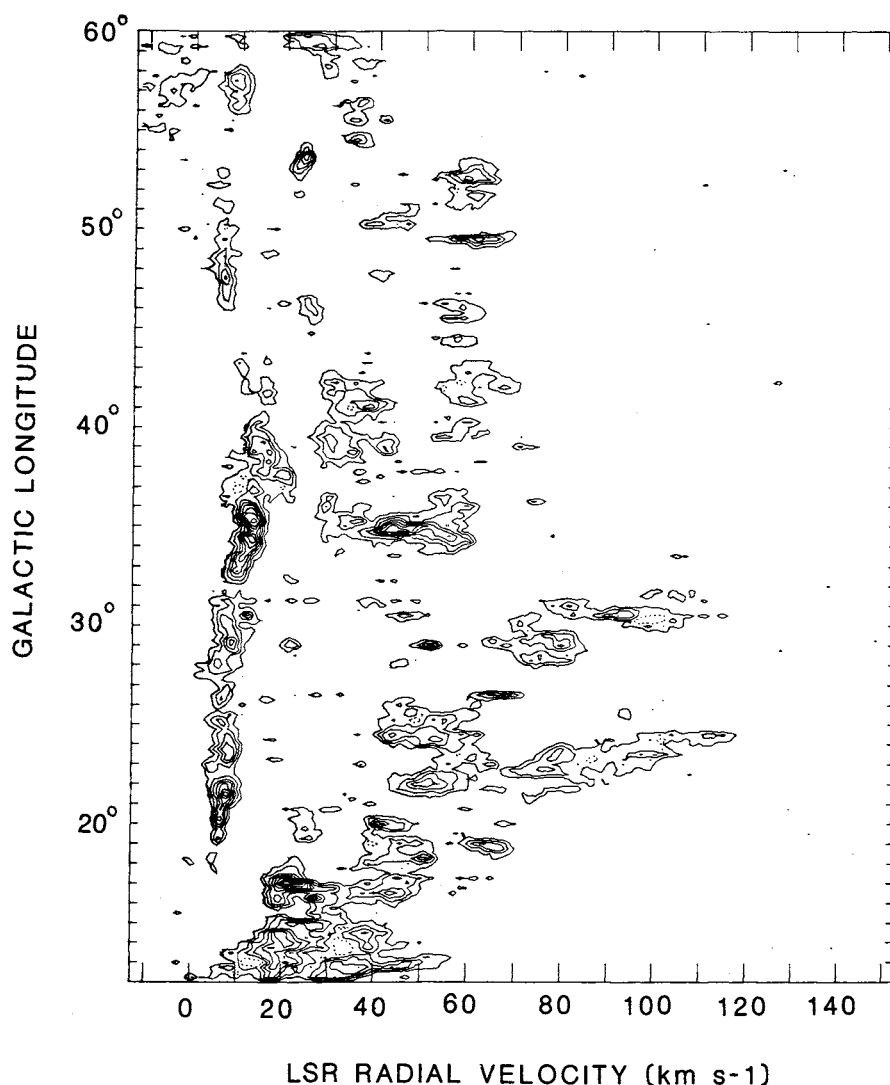


FIG. 11.—Longitude-velocity diagram produced by subtracting our model background from the observed diagram (Fig. 3). The absolute scale of the background model was such that 63% of the emission in the observed diagram at $v > 20 \text{ km s}^{-1}$ was removed in producing this diagram. The diagram has been smoothed in velocity to a resolution of 1.3 km s^{-1} . The contour interval is 0.75 K deg_\circ .

fairly isolated and well defined. The integrated intensities of the complexes were determined directly from a digitized version of Figure 11.

The background model adopted offered a good compromise for the present purpose. A more complicated model, based on the plausible assumption that the background clouds are largely confined to the spiral arms, would greatly increase the number of free parameters, and its use would risk introducing spirality into the data. A simpler model, a completely uniform (l, v) -diagram, would ignore the nature of the transformation from the Galactic plane to the (l, v) -diagram; only a very complicated and completely artificial distribution of emission in the Galactic plane could result in a uniform distribution in the (l, v) -diagram.

The integrated intensities and masses we obtained generally agree, within a factor of 2, with those Myers *et al.* (1986) obtained by using clipping for background removal. For the 33 clouds common to both works, the mean of the mass ratios (Myers *et al.*/this work) is 1.6 ± 0.9 ; the mean of the inverse ratios (this work/Myers *et al.*) is 0.97 ± 0.7 . [Since both works adopt the same distances to the clouds and use the same conversion from $W(\text{CO})$ to $N(\text{H}_2)$, the ratios of the integrated intensities are equal to the ratios of masses; see § IIb.] As expected, the masses Myers *et al.* derived tend to be higher than ours in regions of unusually high background emission. For example, the complexes [24,98] and [31,95] are the most discrepant: the masses determined by clipping are larger by factors of 3.2 and 3.7 respectively than those determined here. These complexes lie both very close to the terminal velocity and near the peak of the molecular ring (see Fig. 2).

Whether clipping or subtraction is the more accurate method of background removal is not entirely clear. A relatively high or low source optical depth might be expected to favor one method over the other, but the optical depth of CO lines in molecular clouds is ambiguous. On one hand, the relative intensity of the CO and ^{13}CO lines in molecular clouds suggests that the CO line is thick, but, on the other, the detailed similarity of the observed line profiles and map structure suggests that integration of the CO line yields a reliable estimate of column density (the mass estimation method used in this paper; see § IIb). Until the physical origin of the CO background is better understood, it would seem unwise to base the choice of clipping versus subtraction on CO optical depth; at present, the differences in the results reflect genuine uncertainty in the masses of the complexes.

APPENDIX C

PREDICTION OF THE MASS DISTRIBUTION OF OUR CLOUD SAMPLE

For the molecular clouds in Table 2 we wish to predict the number and mass distribution and show that these are roughly what would be expected for an apparent-luminosity-limited sample of clouds in the inner Galaxy. As the first step, the total number of clouds as a function of mass is computed from the mass spectrum and total molecular mass of the inner Galaxy. Approximating the molecular cloud mass spectrum by the expression

$$dN(M) = N_0 M^{-\gamma} dM, \quad (\text{C.1})$$

where $dN(M)$ is the number of clouds in a range of mass dM about M , Dame (1983) derived a slope of $\gamma = 1.45 \pm 0.08$ from a section of the Perseus spiral arm, in good agreement with the recent results of Sanders, Scoville, and Solomon (1985) and with Casoli, Combes, and Gerin (1984), all of whom find $\gamma \approx 1.5$.

Integrating equation (C.1) over mass yields

$$M_T = \frac{N_0}{2 - \gamma} M_{\max}^{2-\gamma}, \quad (\text{C.2})$$

where M_T is the total mass of the cloud sample and M_{\max} the mass of the most massive cloud. For the molecular clouds within the solar circle, we take $M_T = 9.1 \times 10^8 M_\odot$, determined from the axisymmetric model fit of Dame (1983),¹ and $M_{\max} = 5 \times 10^6 M_\odot$, the mass of the most massive complex in our sample, which in equation (C.2) yield $N_0 = 10^5$.

With N_0 and γ in equation (C.1) known, it is a simple matter to calculate the number of clouds in any range of mass. The number N_i with masses between M_1 and M_2 is given by

$$N_i = \frac{N_0}{1 - \gamma} (M_2^{1-\gamma} - M_1^{1-\gamma}). \quad (\text{C.3})$$

The number of clouds in half-decade intervals of mass are given under N_{tot} in Table 3.

To calculate the fractions of clouds that will be detected in each half-decade interval of mass, we require S_{\min} , the minimum apparent CO luminosity (in units of $\text{K km s}^{-1} \text{ deg}^2$) a cloud must have to be included in our sample. As evident from Figure 12, where the apparent CO luminosities S of our clouds are plotted as a function of Galactic radius, S_{\min} is not well defined for our sample. In the outer Galaxy (for present purposes, $R > 6.5 \text{ kpc}$) S_{\min} is relatively low, because the overall cloud density is low and even dim clouds appear as distinct emission peaks in the (l, v) -diagram. In the inner Galaxy ($R < 6.5 \text{ kpc}$), the cloud density is higher, as is S_{\min} , because only the most luminous clouds can be distinguished as individual features in the (l, v) -diagram. In the following analysis we adopt different values of S_{\min} for the inner and outer Galaxy.

S_{\min} can be very roughly estimated from Figure 12. A simple estimate of S_{\min} in either region could be S of the dimmest cloud, which, however, should be an underestimation of the average, or effective, S_{\min} , because S_{\min} varies from place to place in the (l, v) -diagram as the background level varies. In the outer Galaxy a fairly clear drop in the number of clouds for $S < 10 \text{ K km s}^{-1} \text{ deg}^2$

¹ Using a mean molecular weight per H_2 molecule of $2.72 m_{\text{H}}$.

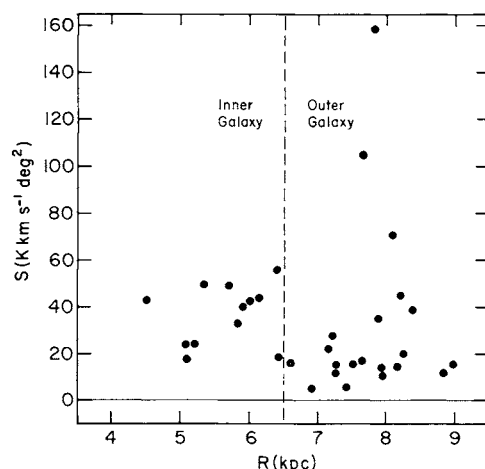


FIG. 12.—The apparent CO luminosity S_{CO} of each complex in Table 2 plotted as a function of its galactocentric radius. The graph demonstrates that complexes with low apparent CO luminosities are detected only in the outer Galaxy.

leads us to adopt 10 and 15 $\text{K km s}^{-1} \text{deg}^2$ as rough lower and upper limits for the average S_{min} in this region. In the inner Galaxy a suitable range for S_{min} is less obvious; the dimmest clouds have $S \approx 20 \text{ K km s}^{-1} \text{deg}^2$, and there is a weak clustering of clouds above 40 $\text{K km s}^{-1} \text{deg}^2$, so here we adopt 25 and 40 $\text{K km s}^{-1} \text{deg}^2$ as lower and upper limits for S_{min} . These limits, although not well determined, are useful to demonstrate the sensitivity of our results to S_{min} .

To calculate N_{exp} we assume that the number surface density of clouds of any mass follows the surface density of the overall CO emission, which, for simplicity, we assume is axisymmetric about the Galactic center with the radial distribution determined by Dame (1983). The fraction of clouds of mass M we expect to detect, $F(M)$, is then $E_0(M)/E_T$, where E_T is the total CO emission within the solar circle and $E_0(M)$ the total CO emission within the area of the Galactic plane over which clouds of such mass could be detected (an area bounded by the longitude limits of our survey and close enough to the Sun that clouds of mass M have $S > S_{\text{min}}$). The quantity $E_0(M)$ can be calculated numerically for any value of M to yield $F(M)$. The numbers given in Table 3 under the heading N_{exp} are simply $N_{\text{tot}} F(M)$, where M is the mean mass of the clouds in the corresponding half-decade mass bin. The low and high values of N_{exp} result from using our upper and lower estimates of S_{min} . Setting $S_{\text{min}} = 0$ yields the number of potentially accessible clouds, N_{acc} in Table 3. The quantity N_{acc} is simply 36% of N_{tot} for all M , since 36% of the total inner Galaxy emission lies within the longitude limits of our survey. (We neglect the few percent of the emission which lie outside our latitude limits; from the wide-latitude survey of Dame and Thaddeus 1985 we know that no large clouds lie at $|b| > 1^\circ$ in this longitude range.)

REFERENCES

- Allen, C. W. 1973, *Astrophysical Quantities* (3d. ed.; London: Athlone).
 Bania, T. M. 1980, *Ap. J.*, **242**, 95.
 Bloemen, J. B. G. M., Caraveo, P. A., Hermsen, W., Lebrun, F., Maddalena, R. J., Strong, A. W., and Thaddeus, P. 1984, *Astr. Ap.*, **139**, 37.
 Bloemen, J. B. G. M., et al. 1986, *Astr. Ap.*, **154**, 25.
 Burton, W. B. 1971, *Astr. Ap.*, **10**, 76.
 Burton, W. B., and Shane, W. W. 1970, *IAU Symposium 38, The Spiral Structure of Our Galaxy*, ed. W. Becker and G. Contopoulos (Dordrecht: Reidel), p. 397.
 Casoli, F., Combes, F., and Gerin, M. 1984, *Astr. Ap.*, **133**, 99.
 Cohen, R. S., Cong, H., Dame, T. M., and Thaddeus, P. 1980, *Ap. J. (Letters)*, **239**, L53.
 Cohen, R. S., Dame, T. M., and Thaddeus, P. 1986, *Ap. J. Suppl.*, **60**, 695.
 Cohen, R. S., Grabelsky, D. A., Alvarez, H., Bronfman, L., May, J., and Thaddeus, P. 1985, *Ap. J. (Letters)*, **290**, L15.
 Cohen, R. S., and Thaddeus, P. 1977, *Ap. J. (Letters)*, **217**, L155.
 Crampton, D., Georgelin, Y. M., and Georgelin, Y. P. 1978, *Astr. Ap.*, **66**, 1.
 Dame, T. M. 1983, Ph.D. thesis, Columbia University.
 Dame, T. M., and Thaddeus, P. 1982, *Bull. AAS*, **14**, 616.
 ———, 1985, *Ap. J.*, **297**, 751.
 Downes, D., Wilson, T. C., Bieging, J., and Winke, J. 1980, *Astr. Ap. Suppl.*, **40**, 379.
 Elmegreen, B. G., and Elmegreen, D. M. 1983, *M.N.R.A.S.*, **203**, 31.
 Elmegreen, B. G., Lada, C. J., and Dickinson, D. F. 1979, *Ap. J.*, **230**, 415.
 Genzel, R., et al. 1981, *Ap. J.*, **247**, 1039.
 Georgelin, Y. M., and Georgelin, Y. P. 1976, *Astr. Ap.*, **49**, 57.
 Kutner, M. L., Tucker, K. D., Chin, G., and Thaddeus, P. 1977, *Ap. J.*, **215**, 521.
 Larson, R. B. 1981, *M.N.R.A.S.*, **194**, 809.
 Lebrun, F., et al. 1983, *Ap. J.*, **274**, 231.
 Leung, C. M., Kutner, M. C., and Mead, K. N. 1982, *Ap. J.*, **262**, 583.
 Liszt, H. S., and Burton, W. B. 1981, *Ap. J.*, **243**, 778.
 Lockman, F. J. 1979, *Ap. J.*, **232**, 761.
 Maddalena, R. J., Morris, M., Moscovitz, J., and Thaddeus, P. 1986, *Ap. J.*, **303**, 375.
 Milne, D. K. 1979, *Australian J. Phys.*, **32**, 83.
 Morris, M., and Rickard, L. J. 1982, *Ann. Rev. Astr. Ap.*, **20**, 517.
 Mufson, S. L., and Liszt, H. S. 1979, *Ap. J.*, **232**, 451.
 Myers, P. C. 1983, *Ap. J.*, **270**, 105.
 Myers, P. C., Dame, T. M., Thaddeus, P., Cohen, R. S., Silverberg, R. F., Dwek, E., and Hauser, M. G. 1986, *Ap. J.*, **301**, 398.
 Sanders, D. B., Scoville, N. Z., and Solomon, P. M. 1985, *Ap. J.*, **289**, 373.
 Sanders, D. B., Solomon, P. M., and Scoville, N. Z. 1984, *Ap. J.*, **276**, 182.
 Schmidt, M. 1957, *Bull. Astr. Inst. Netherlands*, **13**, 247.
 Shane, W. W. 1972, *Astr. Ap.*, **16**, 118.
 Stark, A. A. 1979, Ph.D. thesis, Princeton University.
 Weaver, H. 1970, *IAU Symposium 38, The Spiral Structure of Our Galaxy*, ed. W. Becker and G. Contopoulos (Dordrecht: Reidel), p. 126.

T. M. DAME, R. S. COHEN, and P. THADDEUS: Goddard Institute for Space Studies, 2880 Broadway, New York, NY 10025

B. G. ELMEGREEN: IBM T. J. Watson Research Center, P.O. Box 218, Yorktown Heights, NY 10598

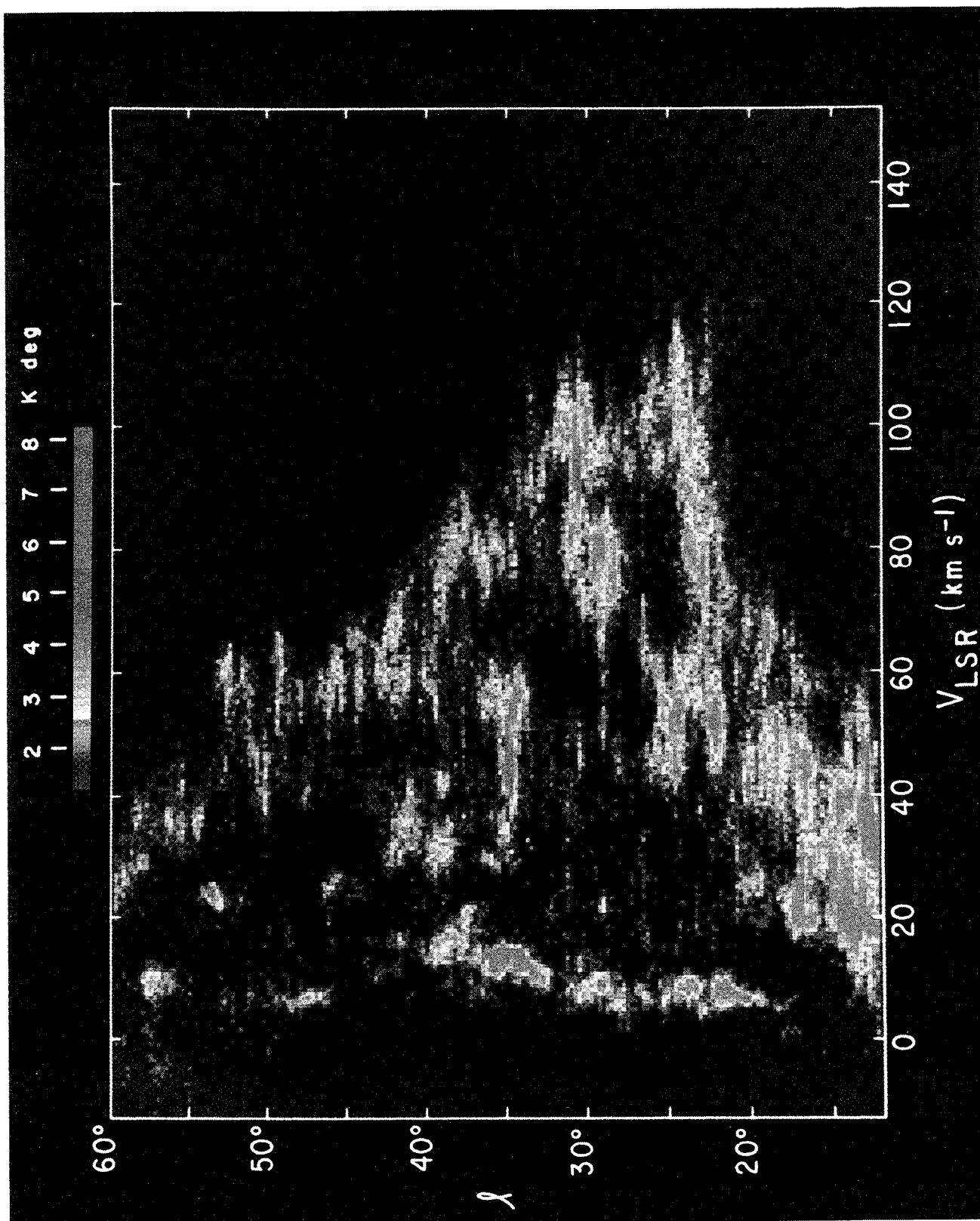


FIG. 3.—False color representation of the longitude-velocity diagram obtained by integrating the Columbia CO survey of the first Galactic quadrant over latitude from -1° to $+1^\circ$. The resolution is 0.25×1.3 km s $^{-1}$.

DAME, ELMGREEN, COHEN, AND THADDEUS (see page 895)